Journal of Materials Chemistry A

Electrocatalytic Selectivity for Nitrogen Reduction vs. Hydrogen Evolution: A Comparison of Vanadium and Cobalt Oxynitrides at Different pH Values

Journal:	*Journal of Materials Chemistry A*
Manuscript ID	TA-ART-06-2022-005180.R1
Article Type:	Paper
Date Submitted by the Author:	31-Aug-2022
Complete List of Authors:	Chukwunenye, Precious; University of North Texas, chemistry Ganesan, Ashwin; University of North Texas, Chemistry Gharaee, Mojgan ; University of North Texas, Chemistry Balogun, Kabirat; University of North Texas, Chemistry Anwar, Fatima; University of North Texas, chemistry Adesope, Qasim; University of North Texas, chemistry Cundari, Thomas; University of North Texas, Chemistry D'Souza, Francis; University of North Texas, Chemistry Kelber, Jeffry; University of North Texas, chemistry

ARTICLE

Electrocatalytic Selectivity for Nitrogen Reduction vs. Hydrogen Evolution: A Comparison of Vanadium and Cobalt Oxynitrides at Different pH Values

Received 00th January 20xx,
Accepted 00th January 20xx

DOI: 10.1039/x0xx00000x

Precious Chukwunenye,[a†] Ashwin Ganesan,[a†] Mojgan Gharaee,[a] Kabirat Balogun,[a] Fatima Anwar,[a] Qasim Adesope,[a] Thomas R. Cundari,[a] Francis D'Souza[a]* and Jeffry A. Kelber[a]

The electrocatalytic nitrogen reduction reaction (NRR) is of significant interest as an environmentally friendly method for NH_3 production for agricultural and clean energy applications. Selectivity of NRR vis-à-vis the hydrogen evolution reaction (HER), however, is thought to adversely impact many potential catalysts, including Earth-abundant transition metal oxynitrides. Relative HER/NRR selectivities are therefore directly compared for two transition metal oxynitrides with different metal oxophilicities—Co and V. Electrocatalytic current-potential measurements, operando fluorescence, absorption, and GC measurements of H_2 and NH_3 production, *ex situ* X-ray photoelectron spectroscopy (XPS), and density functional theory (DFT) calculations are combined to directly compare NRR and HER activities under identical reaction conditions. Results show that cobalt oxynitrides – with Co primarily in the Co(II) oxidation state – are NRR active at pH 10, with electrochemical reduction of both lattice nitrogen and dissolved N_2, the latter occurring without N incorporation into the lattice. Removal of lattice N then yields Co(II) oxide, which is still NRR active. These results are complemented by calculations showing that N_2 binding at Co(II) sites is energetically favored over binding at Co(III) sites. GC analysis demonstrates that H_2 production occurs in concert with ammonia production but at a far greater rate. In contrast, vanadium oxynitride films are HER inactive under the same (pH 10) conditions, as well as at pH 7, but are NRR active at pH 7. DFT calculations indicate that a major difference in the two materials is hindered O-H dissociation of H_2O adsorbed at O-ligated Co vs V cation centers. The combined studies indicate significant variation in HER vs. NRR selectivity as a function of employed transition metal oxynitrides, as well as different HER mechanisms in V and Co oxynitrides.

1. Introduction

Ammonia production is vital to agriculture and feeding a growing world population. Ammonia is also essential for the production of explosives, dyes, and pharmaceutical products, and has recently been proposed as a medium for the storage of hydrogen gas for energy usage.[1] The latter application is expected to cause even higher demand for ammonia when it becomes industrially viable.[2] Ammonia is currently produced by the reduction of molecular nitrogen via the Haber-Bosch process.[3,4] Due to the chemical stability of the N≡N bond,[5] however, the Haber-Bosch process requires high temperatures and pressures to initiate the reaction between H_2 and N_2 to form ammonia, thus consuming between 1 - 2% of the world's energy and producing significant amounts of CO_2.[6]

The alternative process of electrocatalytic reduction of molecular nitrogen to ammonia—the nitrogen reduction reaction (NRR)—is of significant research interest due to the potential for lower energy costs and reduced CO_2 emissions. [5] Numerous electrocatalysts have been proposed, but significant issues include the selectivity and efficiency of NRR catalysts. One competing process that reduces the efficiency of NRR electrocatalysts is the hydrogen evolution reaction (HER), because of relatively similar reaction potentials and the fact that both reactions may possess similar reaction intermediates.[1] To improve the efficiency of NRR, several researchers have tried suppressing HER, but this has proven quite difficult and counterproductive in many cases, as suppression of HER can also cause a simultaneous reduction of NRR activity.[1] Other method employed in making selective NRR electrocatalysts include heteroatom doping, atom vacancy, amorphization, and interfacial polarization. [5,7] [5] One potential method of controlling the competing HER and improving the NRR activity is optimizing the catalyst design and reaction conditions. [1] The latter, of course, requires fundamental studies of variation in HER/NRR selectivity as a function of chemical composition and structure.

[a] *Department of Chemistry, University of North Texas, 1155 Union Circle, #305070, Denton, TX 76203-5017, USA.*
† Contributed equally to this work
* francis.dsouza@unt.edu
Electronic Supplementary Information (ESI) available: [details of any supplementary information available should be included here]. See DOI: 10.1039/x0xx00000x

Transition metal oxynitride (TMON) catalysts have been explored as Earth-abundant electrocatalysts for NRR under various reaction conditions and catalyst morphologies. [8-12] NRR in these materials is often explained as being due to a Mars-van Krevelen (MVK) mechanism, in which N_2 is incorporated as lattice N, followed by lattice N reduction to NH_3. [13,14] However, recent studies on vanadium oxynitride indicate that reduction of lattice N and solvated N_2 occur by separate mechanisms without N_2 incorporation in the lattice, with both reaction pathways energetically favored at O-ligated V centers ($[V]_O$) rather than at N-ligated ($[V]_N$) sites. [15] A notable issue that broadly impacts TMON efficiency for NRR is the apparent competitive nature of the HER. [16-18] An understanding of the relative NRR/HER selectivity for TMONs with different transition metals is thus of practical and fundamental importance. Herein, we present, to our knowledge, the first direct comparison of HER/NRR relative selectivity under comparable reaction conditions for two thin films TMON catalysts of differing metal oxophilicity—Co and V.

This is, to our knowledge, the first demonstration of NRR activity in cobalt oxynitride, although Co(II) and Co(III) oxides have previously been examined for NRR. [19,20] As cobalt oxides are reported to be unstable in solutions with pH < ~ 8, NRR studies on Co oxynitrides were only carried out at pH 10 [21-23]. Comparative studies of V oxynitride were also carried out at pH 10, as well as at pH 7, where our previous studies have demonstrated NRR activity.[15] Relative rates of HER and NRR are assayed by *operando* fluorescence and absorption measurements. *Ex situ* XPS, in concert with such measures, has been used to characterize oxynitride film composition before and after electrocatalysis.

Experimental results are complemented by theory, building upon our previous studies of cobalt and vanadium oxynitride chemical and electronic structure. [24,25] DFT-based calculations demonstrate that the most stable isomers for CoN and CoO_xN_y involve a bridging N_2 arrangement. Oxygen-ligated Co cation centers ($[Co]_O$), with N_2 binding energy of 1.24 eV, form a stronger bond with N_2 than do $[Co]_N$ centers, with a calculated N_2 binding energy of 0.83 eV. All reaction intermediates for distal and alternating NRR pathways ($[Co]\text{-}N_aH_b$, a,b = 1,3) are modeled. Calculations show that CoN and CoO_xN_y models yield similar geometries for the analogous intermediates, which implies that differences in energetics arise from factors other than geometry, *e.g.*, the acid/base properties of the surface-bound dinitrogen adduct. Calculations also shed light on the relative NRR/HER selectivity of oxynitride electrocatalysts as a function of metal (V vs. Co).

Experiments reveal that cobalt oxynitride films are NRR active at pH 10, with both the lattice N and solvated N_2 being reduced to NH_3. As with vanadium oxynitride, lattice N and solvated N_2 reduction occur by independent reaction mechanisms. Time-dependent fluorescence studies, however, demonstrate that H_2 evolves at a rate ~22 times faster than ammonia in the absence of N_2 under these conditions, resulting in facile removal of lattice N from the cobalt oxynitride films, eventually resulting in a Co(II) oxide. DFT-based calculations show that N_2 is more readily bound to a Co(II) site than a Co(III) site, which is consistent with literature reports of NRR enhancement by Al-doping of Co_3O_4.[19, 20]

Similar experiments on vanadium oxynitride at pH 10 reveal that V oxynitride films – similar to those previously examined for NRR at pH 7 [15], are inactive for NRR at pH 10, and inactive for HER at both pH 7 and pH 10. For the first time, these findings demonstrate that HER/NRR relative selectivity can vary substantially with TMON films for different transition metals under identical reaction conditions. Consistent with this finding is the evidence that HER activity for a specific TMON can vary significantly with pH, thus suggesting different HER mechanisms for TMON films comprised of different transition metals.

2. Methods

2.1 Film deposition and analysis

Vanadium and cobalt oxynitride films were deposited in a turbomolecularly-pumped magnetron sputter deposition system (base pressure – 5×10^{-8} Torr) with a commercial DC magnetron source (Meivac, Inc.), as described previously. [15,24,25] Films were deposited on commercially available fluorinated tin oxide (FTO) substrates, 1 cm x 1 cm in size. Vanadium oxynitride films were deposited at a substrate temperature of 675 K, using a plasma pressure of 4 mTorr Ar/N_2 (1:4), 25 W for 7 min. Prior to film deposition, the substrates were annealed in oxygen at 10^{-6} Torr to 900 K for 3 h to remove adventitious C and other contaminants. Cobalt oxynitride films were deposited at room temperature at a pressure of 4 mTorr Ar/N_2 (1:4), 25 W for 20 mins. The gases used were all electronic grade and were used without further purification. Vanadium (purity 99.9%) and cobalt (99.5%) sputter targets (1.3 inches diameter) were used as the metal sources; the substrate-to-sample distance was 3 inches. Although the film thicknesses were not measured directly, previous experiments using similar deposition parameters have yielded films that are ~500 Å thick. [15,26] *In situ* analyses of atomic ratios were done using a commercial Auger single-pass cylindrical mirror analyzer with a concentric electron gun (ESA 100; STAIB Instruments). Auger spectra were recorded at a 3 keV electron beam energy.

After sputter deposition and characterization, the samples were transferred in ambient to a second vacuum chamber system for XPS analysis. [27] XPS spectra were obtained in the constant pass energy mode (23.5 eV) using a commercial 140 mm hemispherical analyzer (Physical Electronics) with a micro-channel plate detector and Al Kα radiation from an unmonochromatized source operated at 300 W and 15 keV. Analysis of XPS data was carried out by standard methods.[28] Peak fitting employed Gaussian−Lorentzian components and was carried out as described previously. [15,24] XPS binding energies were calibrated to C 1s at 284.8eV. [29]

Some films were selected for further characterization by atomic force microscopy (AFM), X-ray diffraction (XRD) and scanning electron microscopy (SEM). AFM studies were carried out at the UNT Materials Research Facility using a VEECO Multimode Nanoscope III AFM in tapping mode with a tip force constant of 40 N/m. X-ray diffraction (XRD) 2θ scans were also

obtained for several films using a Rigaku Ultima III Instrument employing Cu Kα radiation (λ = 1.541 Å). Scanning electron microscopy/energy-dispersive X-ray spectroscopy (SEM/EDX) data were obtained using an FEI Quanta 200 ESEM in high vacuum mode ($1.18x10^{-6}$ Torr) with Everhardt-Thornley detector. EDX take-off angle was set at 35^0 and spectra was acquired using EDAX Element SDD, 25mm^2 Si_3N_4 window, and TEAM software.

2.2 Electrochemical measurements

Samples were transferred in ambient for electrochemical measurements. A three-electrode electrochemical cell was utilized. Studies at pH 10 were conducted in 0.05 M aqueous phosphate buffer. Electrochemical measurements at pH 7 were carried out in 0.1 M Na_2SO_4, as described previously.[15] Before each experiment, the system was saturated with either N_2 or Ar. Electrochemical measurements were performed with an EG&G 263A potentiostat/galvanostat with Ag/AgCl reference electrode and Pt wire counter electrode. Linear sweep voltammetry measurements were performed in the cathodic direction for the oxynitride films deposited on FTO glass. Control studies were also done on bare FTO to understand the behavior of the FTO substrate. Multicyclic voltammograms (15 cycles) were recorded on selected samples under the same working environment to gain insight into the stability of films. N_2 from the gas line, used as the main contributor to ammonia production, is passed sequentially through 2 traps containing 0.1 M HCl and 0.1 M KOH to eliminate possible contamination from NH_3, NO_2^-, and NO_3^-.

Bulk electrolysis measurements were performed under an N_2 atmosphere on 1 cm^2 cobalt oxynitride films to produce ammonia. Electrolysis was performed using 20 mL of 0.05 M phosphate buffer (pH = 10) for 1.5 hr at a potential of -1.1 V vs Ag/AgCl. After the experiment, 10 mL of the electrolyte was removed and mixed with 0.5 mL of 0.55 M NaOH containing 5 wt% salicylic acid and sodium citrate, 100 µL of sodium nitroprusside dehydrate, and 100 µL of sodium hypochlorite to generate indophenol blue dye from the ammonia formed during the bulk electrolysis experiment. [26] After keeping the solution at room temperature for ~30 min, the absorbance of the dye was measured using a JASCO V-670 spectrophotometer. When matched with the absorbance data of the commercial indophenol blue dye, the obtained absorbance revealed similar spectral characteristics. The remaining 10 mL of the electrolyte after electrolysis was treated with the working reagent (WR) formed by mixing sodium sulphate (1 g in 125 mL water), borate buffer (80 g in 2 L water), and orthophthadialdehyde (4 g in 100mL of ethanol). [30] The resultant mixture was stored in the dark for 1 hour, and fluorescence measurements were carried out using a Horiba Jobin Yvon Nanolog UV-visible-NIR spectrofluorometer.

For the detection of hydrazine (N_2H_4), the standard Watt and Chris method was used.[46] A 'color reagent' was developed by the reaction of *p*-dimethylaminobenzaldehyde, ethanol, and conc. HCl. The yellow color developed upon the reaction of the color reagent with hydrazine was quantified by monitoring the absorption at 457 nm. The procedure was standardized by using commercial hydrazine prior to using it to detect N_2H_4 in the bulk electrolyzed solution.

C. Calculations

Density functional theory (DFT) was used within the Vienna Ab initio simulation package.[31] An exchange-correlation (XC) functional and appropriate pseudopotentials replaced nuclei and core electrons. All simulations were spin-polarized and implemented the generalized gradient approximation (GGA) and projector-augmented wave (PAW) methods. [32] The Brillouin zone was sampled using the Monkhorst–Pack scheme. [33]

A major goal of this project is to better understand the roles of lattice N and lattice O in the reduction of nitrogen to NH_3 with cobalt oxynitride electrocatalysts. Free energy calculations were therefore used to calculate N_2 absorption energies at Co sites for CoN and CoO_xN_y models, as well as subsequent hydrogen transfer to surface-bound N_2 in these models. Because the modeled reactions happen on the surfaces of catalysts, the energy-cutoff and K-point mesh were increased to 500 eV and 3 x 3x 1, respectively, to obtain more accurate surface energies, and the size of the supercell was increased in the c direction – from whence the adsorbates bind – in order to remove interactions between surface unit cells until the energy converged to 1 meV. To avoid the interaction of periodic images, the computation has a vacuum space of 20 Å (c lattice constant ~ 29 Å). The bottom three atomic layers of the CoN and CoO_xN_y slabs were fixed, and the top five atomic layers and absorbed groups were relaxed.

Two models for cobalt oxynitride surfaces in zincblende structures were utilized. For both structures, the most stable (110) Miller-index facet was selected [34] to build simulation models for surface DFT calculations. For the first model, the surface layer was cobalt, and the second layer nitrogen; these layers were then repeated. The slab model had 8 layers in total and was intended to mimic zb-CoN. A related model with a surface layer of cobalt and a second layer of oxygen followed by alternating layers of Co and N (8 layers in total, as before) was used to mimic CoO_xN_y that was O-rich at the surface. Both models had a unit cell of 8.09 x 8.09 x 28.79 Å.

3. Results

3.1 Cobalt oxynitride films

In-situ AES spectra showed the presence of cobalt and nitrogen after deposition and the presence of oxygen after ambient exposure, as shown in Fig. S1(Supplementary Information). The N/O atomic ratio after ambient exposure was calculated to be 0.4 based on AES spectra. XPS data taken after deposition and subsequent additional ambient exposure (Fig. S2, Supplementary Information) showed that this film composition was $CoO_{0.8}N_{0.2}$. While such sample handling might be expected to produce a cobalt oxide layer on top of a nitride substrate, the XPS spectra acquired in grazing emission (Fig. S2, red-- surface sensitive, with analyzer inclined 60^0 with respect to the sample normal) and normal emission (Fig. S2, green—normal emission; analyzer aligned with the sample normal) show a negligible

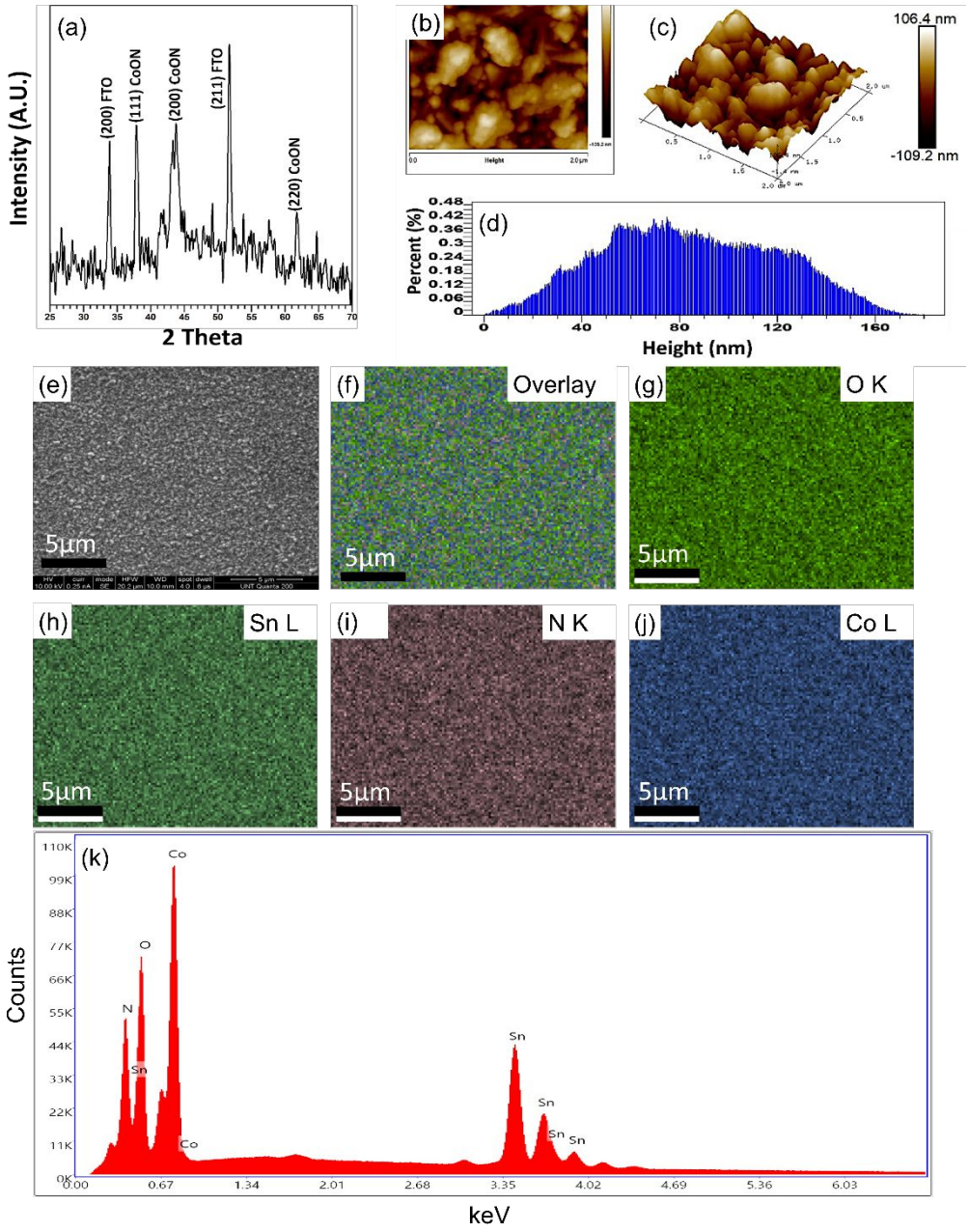

Figure 1 – Characterization of CoO0.8N0.2 films deposited under similar conditions as films used for electrochemical studies. In-situ AES spectra were similar for all these films – (a) XRD; (b) 2D & (c) 3D AFM images; (d) depth histogram; SEM-EDX (e) image (f) element overlay and elemental mapping for (g) oxygen (h) tin (i) nitrogen & (j) cobalt content; (k) EDX analysis spectrum

difference in core level spectra, consistent with a uniform Co oxynitride film. Furthermore, the core level spectra in both cases resemble those reported previously. [24]

A grazing incidence X-ray diffraction scan of a similarly synthesized $CoO_{0.8}N_{0.2}$ film (Fig. 1a) showed cobalt oxide nitride peaks – CoON(111), CoON (200), and other features shown in Fig. 1a. No features corresponding to, for example, cobalt metal or oxide phases were observed, indicating that the deposited films are homogeneous and polycrystalline in nature, rather than amorphous. AFM measurements showed a surface roughness of 35.2 nm (Fig. 1b-d), approximating that of the FTO substrate[15]. All films used for experiments were deposited using similar parameters and had similar atomic ratios as determined from *in-situ* AES and *ex-situ* XPS data. Scanning electron microscopy/energy dispersive spectroscopy studies of a $CoO_{0.8}N_{0.2}$ film are shown in Fig. 1(e-k). These show the uniform elemental composition of the films.

A Co oxynitride film with XPS-derived composition $CoO_{0.8}N_{0.2}$ was selected for EC studies of NRR. At pH 10, using 20 mL of 0.05 M phosphate buffer, this film displayed higher currents when the solution was saturated with N_2 gas than when it was saturated with Ar gas, as shown in Fig. 2a. Ammonia production was detected using the indophenol blue method (shown in Fig. 2b) for cathodic polarization of the film in both Ar- and N_2-saturated solutions. The data in Fig. 2b confirm that a greater ammonia concentration was detected in the N_2-

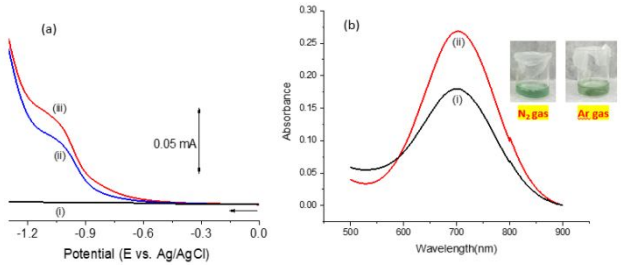

Figure 2 - (a) Polarization curves for the (i) blank FTO electrode in the N_2-saturated solution, (ii) $CoO_{0.8}N_{0.2}$ film on the FTO electrode in an Ar-saturated 0.05 M phosphate buffered solution at pH 10, and (iii) same $CoO_{0.8}N_{0.2}$ film electrode in 0.05 M phosphate buffered solution at pH 10 in the N_2-saturated solution. (b) Absorbance spectrum (i) after electrochemical polarization of a $CoO_{0.8}N_{0.2}$ film in the Ar-saturated solution, and (ii) after electrochemical polarization of said film in the N_2-saturated solution.

saturated solution than in the Ar-saturated solution. Taken together, these results indicate that both lattice N and solvated N_2 are being reduced in the cobalt oxynitride catalyzed NRR reaction to NH_3 in solution at pH 10. Corresponding XPS data acquired after polarization in Ar-saturated show such EC polarization depletes N from the Co oxynitride film as shown in Fig. S3.

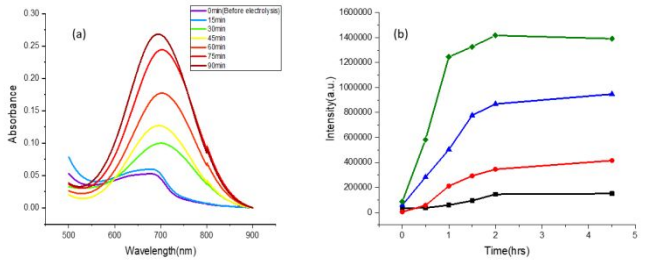

Figure 3 - (a) Time-dependent absorption spectrum upon electrochemical polarization of a $CoO_{0.8}N_{0.2}$ film in the N_2-saturated solution. (b) Fluorescence intensities with time plotted for working reagent (WR, black trace), (ii) WR combined with the electrolyte before electrolysis (red trace), (iii) WR combined with electrolyte after electrolysis of $CoO_{0.8}N_{0.2}$ film under argon environment (blue trace) and under nitrogen environment (green trace).

Time-dependent absorption measurements of a similar film (composition $CoO_{0.8}N_{0.2}$ - as determined by XPS), displayed in Fig. 3a, indicate a gradual increase in the absorbance of the dye formed, and therefore NH_3 production, with respect to time. The overall time dependence for NH_3 production, as determined by fluorescence measurements (Fig. 3b), is similar in both N_2- and Ar-saturated solutions, though more significant in the former. However, in both cases, NH_3 production appears to cease after ~2 hours of electrolysis under these conditions, which could perhaps signify the end of the reduction of nitrogen in the lattice to ammonia, and/or formation of an NRR-inactive Co (III) oxide phase.

To detect the formation of H_2 from any simultaneously occurring hydrogen evolution reaction, gas chromatography was used to detect the concentration of H_2 in the solution at

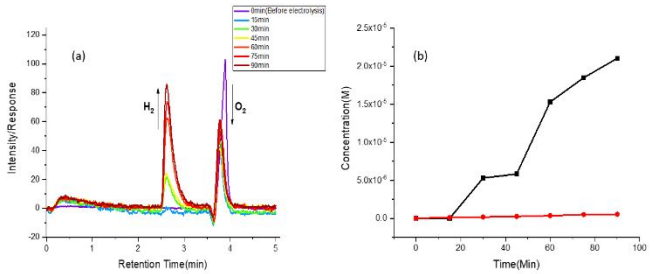

Figure 4 - (a) Time-dependent gas chromatogram for the hydrogen evolution reaction (HER); (b) concentration of ammonia (red trace) and hydrogen (black trace) produced plotted versus time on a $CoO_{0.8}N_{0.2}$ film in N_2-saturated solution.

intermittent intervals, as shown in Fig. 4. These measurements were made on a fresh film of similar composition as the above ($CoO_{0.8}N_{0.2}$). This step was taken in order to compare HER and NRR measurements on fresh films of similar composition, as XPS measurements (see below) demonstrated significant changes to film surface composition during EC polarization. The gas chromatography-thermal conductivity detector (GC-TCD) peak at 2.62 min (Fig. 4a) is attributed to the presence of hydrogen, while a peak at 3.68 min is attributed to oxygen. Oxygen production decreases significantly with time (Fig. 4a), suggesting either a surface or solution impurity. A gradual increase in the concentration of H_2, however, was observed over the course of the experiment, which indicates significant production of H_2. The time dependencies of NH_3 and H_2 production for this film are compared in Fig. 4b. This shows that hydrogen is produced at a significantly faster rate than ammonia under these experimental conditions.

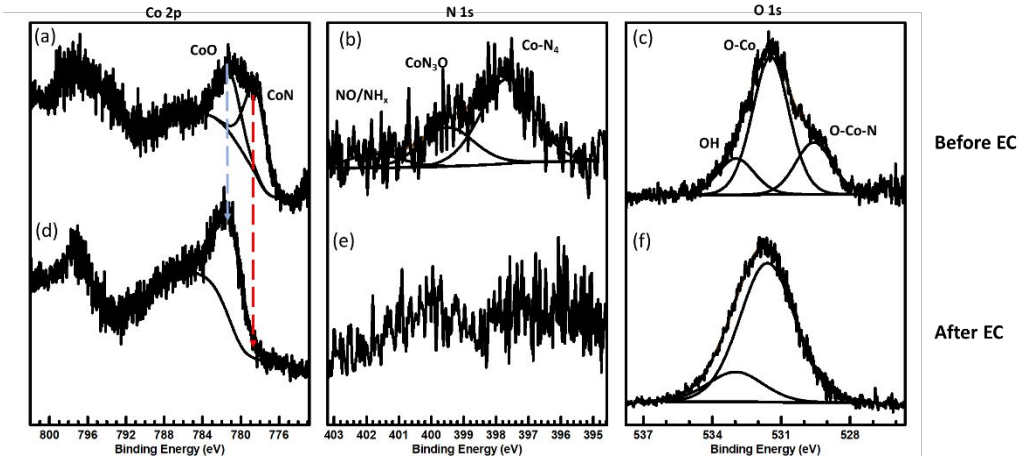

Figure 5 - XPS of $CoO_{0.8}N_{0.2}$ film before/after EC in presence of N_2 This shows that lattice N is lost during cathodic polarization.

XPS spectra of Co oxynitride surface composition were obtained for a $CoO_{0.8}N_{0.2}$ film (the same as in Fig. 2) before and after electrochemical measurements in Ar- and then N_2-saturated solution, and these XPS spectra are displayed in Fig. 5. The Co 2p XPS data acquired prior to EC polarization (Fig. 5a) show a feature near 780 eV binding energy attributable to Co(II) oxide[35] and a sharp feature near 778 eV attributable to Co-N bonding.[24] N 1s data (Fig. 5b) demonstrate the presence of a broad N 1s feature attributable to Co-N and O-Co-N interactions.[24] Corresponding XPS data (Figs. 5d-f) were acquired after polarization in Ar-saturated and then N_2-saturated solution, followed by emersion at -1.06 V vs. Ag/AgCl and rinsing in DI H_2O. However, these data show that such EC polarization depletes N from the Co oxynitride film within the N 1s sampling depth, which is approximately twice the calculated N 1s inelastic mean free path of 9.5 Å through CoO. [36] The XPS data in Figs. 5d-f indicate that, after extensive EC polarization, the film composition is essentially CoO.

The XPS data in Fig. 5 are consistent with the conclusion that lattice nitrogen is reduced to ammonia and that subsequent reaction of the N-depleted film with N_2 results in additional NH_3 formation. This corroborates previous reports in the literature[20] reporting that CoO is NRR-active under alkaline conditions. However, the data in Fig. 5 also indicate that reduction of solvated N_2 does not result in significant N incorporation into the lattice under these conditions, as might be expected for NRR operating via an MVK mechanism.

Table 1. NRR Comparison, CoO and Co oxynitride

Material	Onset potential (vs. Ag/AgCl)	Faradaic Efficiency	NH_3 yield ($\mu g h^{-1} mg_{cat}^{-1}$)
CoO	-0.77 V	0.97%	123.94
$CoO_{0.8}N_{0.2}$	-0.59 V	1.52%	168.81

Taken together, the data in Figs. 2 - 5 indicate that Co oxynitride films are active for both nitrogen reduction and hydrogen evolution reactions at pH 10, resulting in the depletion of lattice N, but with H_2 produced at a significantly higher rate than N_2.

NRR measurements, including onset potential, FE and NH3 yield, were compared to the $CoO_{0.8}N_{0.2}$ film (as in Fig. 5) before and after N depletion (yielding CoO), under identical experimental conditions. The results, summarized in Table 1, clearly show that the presence of lattice N results in a lower onset potential, corroborating the existence of a separate reduction mechanism for lattice N than for N_2. The higher NH_3 yields and FE values are also indicative of two parallel pathways for lattice N and NH_3 reduction, in contrast to the commonly accepted MVK mechanism. In this respect, the results for Co oxynitrides are similar to those previously observed for V

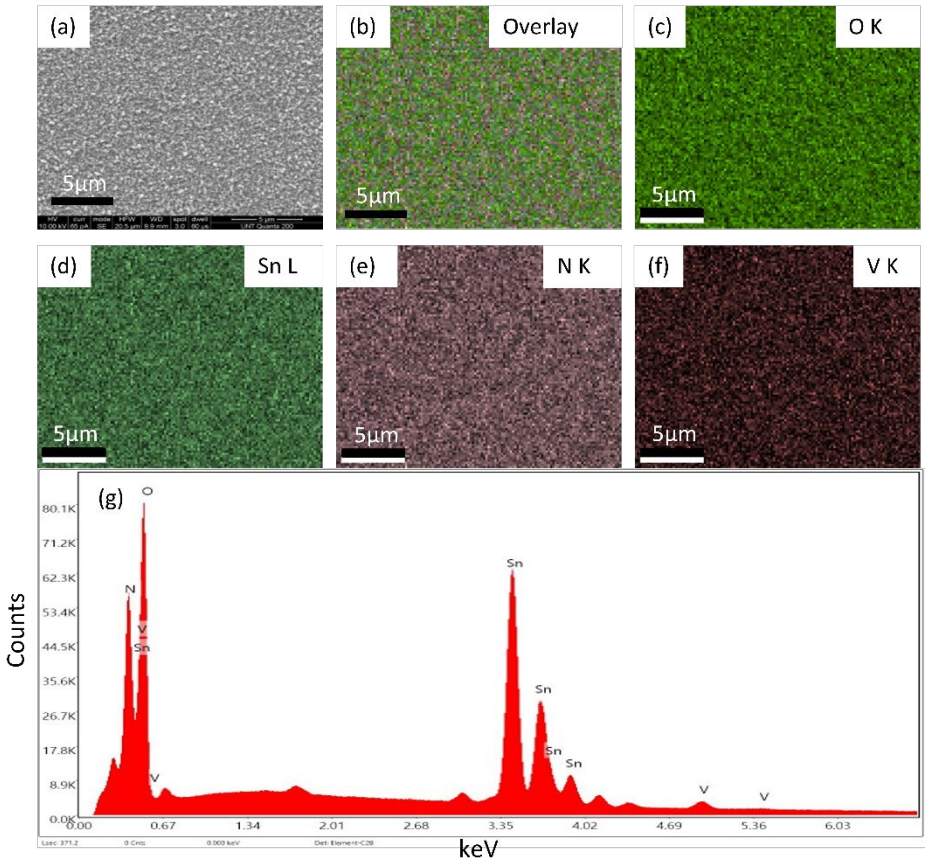

Figure 6 – SEM-EDX (a) image (b) element overlay and elemental mapping for (c) oxygen (d) tin (e) nitrogen & (f) vanadium content of a magnetron sputter deposited vanadium oxynitride film; (g) energy-dispersive x-ray analysis (EDX) spectrum

oxynitrides [15], indicating that there is no NRR-related MVK mechanism for these materials.

"NRR measurements, including Onset potential, FE, and NH_3 yield, were compared to the $CoO_{0.8}N_{0.2}$ film (as in Fig. 5) before and after N depletion, under identical experimental conditions. The results, summarized in Table I, clearly show that the presence of lattice N results in a lower onset potential, corroborating the existence of a separate reduction mechanism for lattice N than for N_2. The higher NH_3 yields and FE values are also indicative of two parallel pathways for lattice N and NH_3 reduction, in contrast to the commonly accepted MVK mechanism. In this respect, the results for Co oxynitrides are similar to those previously observed for V oxynitrides,[15] indicating that there is no NRR-related MVK mechanism for these materials."

Further, detection of N_2H_4 (see the experimental section for details), as one of the possible reaction intermediates, was also performed. Such analysis resulted in no measurable amounts of hydrazine for the bulk electrolyzed product of CoON+N_2 in phosphate buffer at pH = 10.

3.2 Vanadium oxynitride films

Characterization (AFM, XRD, XPS) of V oxynitride films deposited by DC magnetron sputtering in this manner has been described previously. [15] Ex-situ AES spectra are shown in Fig. S4 and correspond to a composition (after ambient exposure) of $VO_{0.4}N_{0.6}$. SEM/EDX spectra of a $VO_{0.3}N_{0.7}$ film are shown in Fig. 6. The data in Fig. S4 indicate that ambient exposure induces negligible changes in V/O/N atom ratios, while the SEM data in Fig. 6 indicate a spatially uniform elemental composition.

NRR activity of these films at pH 7 was also described. [15]

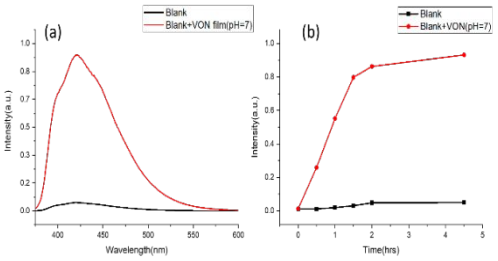

Figure 7 - (a) Fluorescence spectrum of a $VO_{0.4}N_{0.6}$ film in N_2-saturated solution at pH 7 before and after 4.5 hr bulk electrolysis; (b) fluorescence intensities against time for blank FTO and film during 4.5 hr of bulk electrolysis.

However, we have included here time-dependent fluorescence studies as an additional quantitative measurement to corroborate the previously reported indophenol blue results. The films discussed here had identical compositions of $VO_{0.4}N_{0.6}$ as determined by AES. As shown in Fig. 7, there is a sharp increase in the ammonia produced by a $VO_{0.4}N_{0.6}$ film relative to that produced by an unmodified FTO electrode when bulk electrolysis is done at -0.8 V vs. Ag/AgCl in N_2 saturated solution. These results agree with the previously reported results on vanadium oxynitride films of varying N/O compositions being NRR active at pH 7. [15]

To evaluate the evolution of hydrogen, time-dependent GC measurements were carried out using the same film at pH 7 at a potential of -0.8 V vs. Ag/AgCl electrode in N_2-saturated

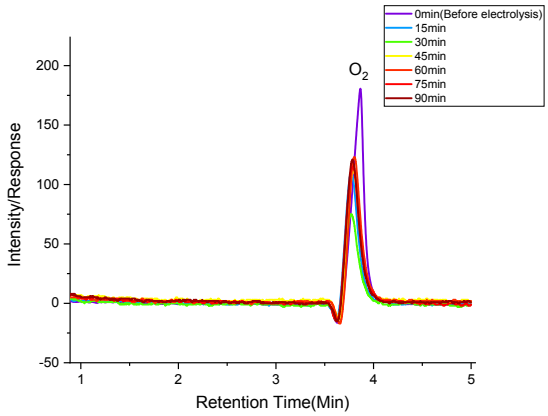

Figure 8 - Time-dependent GC measurements showing the absence of hydrogen for a $VO_{0.4}N_{0.6}$ film at pH 7; same film as in Fig. 7.

solution as shown in Fig. 8. No hydrogen was observed in the GC-TCD measurements indicating there was no concurrent HER occurring in the vanadium oxynitride catalyzed NRR solutions. Using indophenol blue and fluorescence measurements, a different film deposited with the same surface composition ($VO_{0.4}N_{0.6}$) was tested for NRR activity at pH 10. Linear sweep voltammetry recorded at pH 10 in 0.05 M aqueous phosphate buffer under an N_2 environment showed considerable change in current when compared to the blank solution. However, indophenol blue test and fluorescence results after bulk electrolysis is done at -0.8 V vs. Ag/AgCl for 90 min showed that negligible amounts of ammonia were formed at pH 10, Fig. 9. Similar to the results at neutral pH, GC experiments after bulk electrolysis at -0.8 V vs. Ag/AgCl showed that hydrogen was not detected (Fig. S5). The higher total current shown in Fig. 9a for the $VO_{0.4}N_{0.6}$ film compared to the blank FTO sample, in the absence of significant NH_3 production (Fig. 9b), or HER (Fig. 8) , indicates that other electrochemical processes are occurring. One of these is certainly O_2 evolution (Fig. 8), but other, as yet undetermined processes cannot be excluded based on the available evidence.

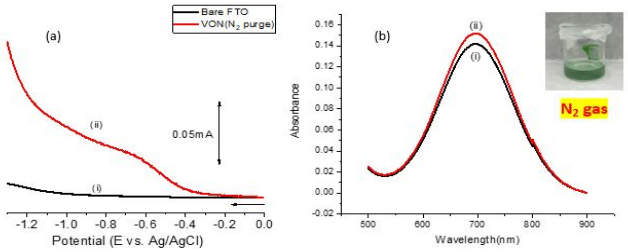

Figure 9 - (a) Polarization curves for blank FTO and $VO_{0.4}N_{0.6}$ film in N_2-saturated 0.05M of phosphate buffered solution at pH 10; (b) absorbance spectrum before (i) and after (ii) electrochemical polarization of bare FTO and VON film in N_2-saturated solution.

In summary, vanadium oxynitride films were active for NRR at pH 7 and mostly inactive at pH 10. However, they were HER inactive at both pH 7 and pH 10.

3.3 Comparison of different models of attaching N_2 to zb-CoN and zb-CoO_xN_y surfaces

Models for cobalt-terminated cobalt nitride(110) and cobalt oxynitride(110) in the zincblende structure were built as described above in computational methods. It was first sought to identify the most stable among various linkage isomers for N_2 bound to the surface models and to assess the energetics of the reactions in eqs. i and ii. DFT-based calculations were thus performed. The linkage models examined include (i) N_2 bonded end-on between two Co atoms (Fig. 10a, left); (ii) N_2 bonded side-on between two Co sites (Fig. 10a, center); and (iii) N_2 bonded end-on to a single Co atom (Fig. 10a, right).

i. zb-CoN+ N_2 → zb-CoN-N_2 → ½ N_2 + zb-CoN-N

ii. zb-$CoO_{0.44}N_{0.56}$ + N_2 → zb-$CoN_{0.44}O_{0.56}$ - N_2 → ½ N_2 + zb-$CoN_{0.44}O_{0.56}$-N

The calculated energies for these three *N_2 models (* indicates a surface site) were very similar, with computed energies within ~0.1 eV of each other upon geometry optimization. Figure 10 shows that after removing one nitrogen from each of the three *N_2 configurations, two nitride isomers were produced (bridging and terminal) for both CoN and $CoO_{0.44}N_{0.56}$ models (Fig. 10A). There were large free energy differences between the terminal and bridging *N models, with the latter being much more favorable for both cobalt nitride and cobalt oxynitride models. Based on a calculated energy difference of ~0.7 eV (Table 2), the formation of *N from

Table 2 - Calculated reaction energies (in eV) of bond scission (columns 2 and 4) and binding (columns 3 and 5) of surface-dinitrogen for zb-$CoO_{0.44}N_{0.56}$ and zb-CoN models. See eqs. i and ii.

	zb-CoN		zb-$CoO_{0.44}N_{0.56}$	
N_2 position on the surface	E(N-remove) eV	Binding E surface-N_2	E(N-remove) eV	Binding E surface-N_2
_CoN_2	2.64	-0.93	2.21	-1.24
CoN_2Co	1.30	-0.83	0.56	-1.24
CoNNCo	2.66	-0.95	0.74	-1.17

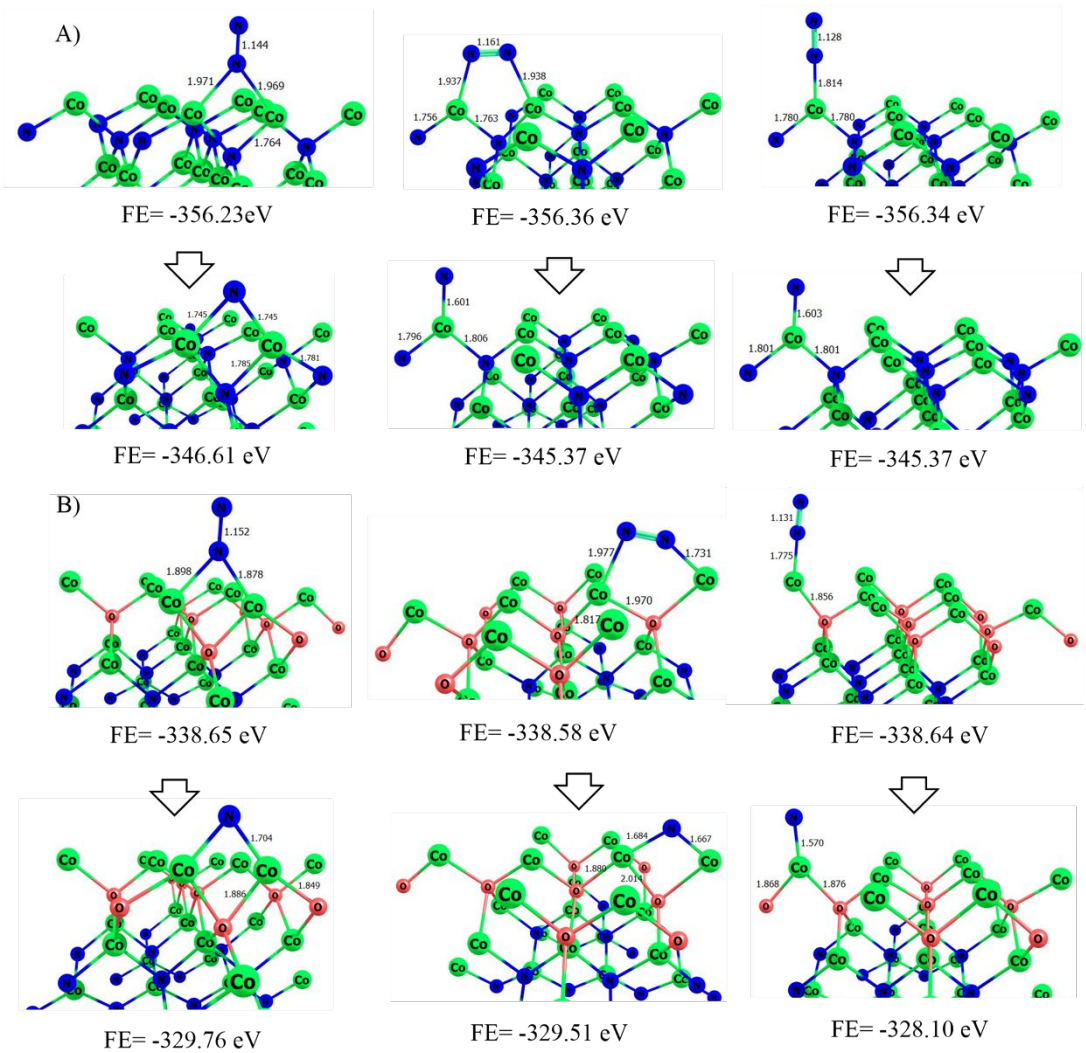

Figure 10 - Three linkage isomers of *N_2 and the surface nitrides generated therefrom on (a) CoN and (b) $CoO_{0.44}N_{0.56}$ surface models with relative free energy in eV. Co, O and N atoms are represented by green, red and blue spheres, respectively. Co, N and O sites atoms are represented by green, blue and red spheres, respectively.

adsorbed N_2 (eqs. ii) is energetically more favored at $[Co]_O$ versus $[Co]_N$ sites in cobalt oxynitride.

Based on the DFT results, the most stable $*N_2$ configuration for both CoN and CoO_xN_y models are those with dinitrogen bonded to two Co sites although the linkage isomers are close in energy. Note that the optimized NN bond lengths (Fig. 10A: 1.14 Å, 1.16 Å, and 1.12 Å; Figure 10B: 1.15 Å, 1.16 Å, and 1.13 Å, respectively) are considerably longer when bonded to the surface models than the 1.09 Å nitrogen-nitrogen bond length calculated for optimized N_2(g) at the same level of theory, indicative of dinitrogen activation upon coordination to the surface cobalt ions.

3.4 Modeling of $[Co]\text{-}N_aH_b$ surface intermediates

The general mechanism of the NRR process is typically comprised of four processes: (i) adsorption of dinitrogen on the catalyst surface (discussed in the previous section), (ii) activation of the dinitrogen triple bond by either transfer of a proton from a proton donor or injection of an electron through external current, (iii) the subsequent proton-coupled electron transfer (PCET) steps, and eventually (iv) ammonia formation. In the distal mechanism, hydrogen is first transferred to the outside nitrogen (furthest from the catalyst surface) of $*N_2$ to produce an equivalent of ammonia, then the inside nitrogen is reduced to a second equivalent of ammonia. On the other hand,

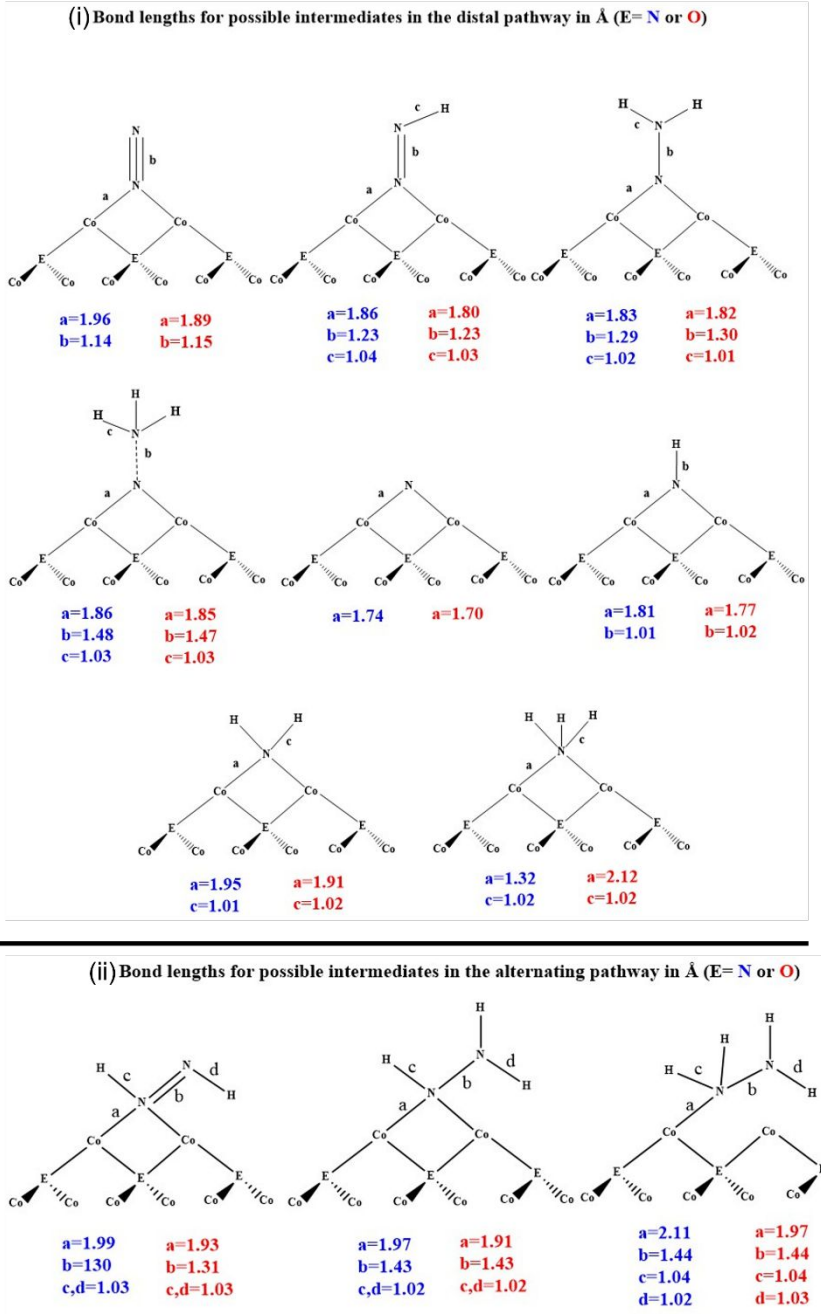

Figure 11 - Co-N, N-N and N-H bond length in Å of various surface configurations of N/H intermediates in NRR for both distal (i) and alternating (ii) pathways E = O (red), $[Co]_O$, and E = N (blue), $[Co]_N$.

for the alternating pathway, hydrogen is first attached to the inner nitrogen of $*N_2$, then the outer nitrogen of the *NNH thus formed to yield surface-bound diazene, and then back and forth between them to eventually produce 2 equivalents of ammonia from $*N_2$.

DFT calculations were done for plausible reaction intermediates on both $CoO_{0.44}N_{0.56}$ and CoN surface models to test the roles of $[Co]_O$ and $[Co]_N$ centers, respectively. Fig. 11 shows schematically the surface configurations of $[Co]\text{-}N_aH_b$ (a = 1 or 2, b = 1, 2 or 3). In Fig. 11, the free energies relative to surface-bound N_2 are calculated and compared for these configurations, E (ligand) = O (red) or N (blue).

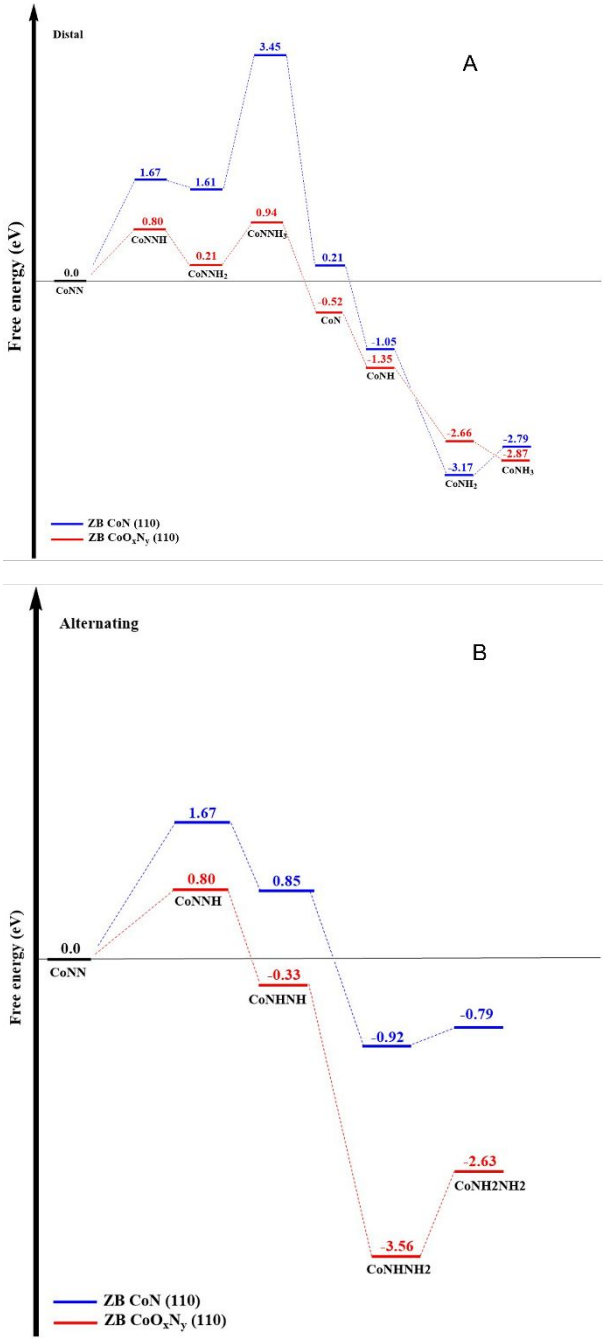

Figure 12 - Various surface configurations of N/H intermediates in NRR for distal (A) and alternating (B) pathways. Calculated relative free energies (in eV), E = O (red), $[Co]_O$, and E = N (blue), $[Co]_N$.

The results summarized in Fig. 11 (i) indicate that when dinitrogen attaches to an electrocatalyst model surface, the dinitrogen bond length increases from 1.09 Å to 1.14 Å for $[Co]_O$, and to 1.15 Å for $[Co]_N$. Furthermore, $[Co]_O$ binds N_2 more tightly than does $[Co]_N$, as evidenced by optimized Co-N bond lengths of 1.89 Å and 1.96 Å, respectively. One may further conclude that $[Co]_O$ with an N_2 binding energy of 1.24 eV (zb-CoO_xN_y model) forms a stronger bond with N_2 in comparison to the calculated binding energy of 0.83 eV for $[Co]_N$ (zb-CoN model).

For intermediates in the distal pathway, Fig. 11(ii), the first hydrogen bonds to the outer nitrogen of $*N_2$, which causes Co-N bond shortening by ~0.1 Å in *NNH; the optimized nitrogen-nitrogen N bond length is longer than that in $*N_2$ by a similar amount. These trends in CoN and NN bond lengths continue for other intermediates until the first ammonia is made (Fig. 11). After that, bonding hydrogen to the inner nitrogen makes Co-N bond lengths longer (Fig. 11). On the other hand, for intermediates in the alternating pathway (Fig. 11), the Co-N bond lengths keep increasing upon attaching further hydrogen atoms.

Calculated free energies for the distal and alternating NRR pathways are shown in Figs. 12A and 12B, respectively. Upon comparing the energy of $*N_aH_b$ isomers with the same number of hydrogens transferred for both distal and alternating pathways, the first hydrogen is predicted to bond to the outer nitrogen of adsorbed dinitrogen to make surface-bound diazenide, *NNH. After that, the second hydrogen attaches to the inner nitrogen of *NNH to form *NHNH (diazene adduct) with relative (to $*N_2$) energies of 0.85 eV for $[Co]_N$ and -0.33 eV for $[Co]_O$ for the alternating pathway, Fig. 12b.

The third hydrogen is predicted to continue the alternating pathway leading to the $*NHNH_2$, hydrazide (1-), intermediate which has a weak NN single bond 1.43 Å with the most stable isomer for $[Co]_O$ E_{rel} = -3.56 eV energy and E_{rel} = -0.92 eV for $[Co]_N$. The relative energies of other isomeric species generated by the addition of three hydrogens to $*N_2$, *i.e.*, $*N—NH_3$ and *N + NH_3(g), are higher in energy with calculated E_{rel} = 0.94 eV for $[Co]_O$ and 3.45 eV for $[Co]_N$ for the $*N—NH_3$ isomer and E_{rel} = -0.52 eV for $[Co]_O$ 0.21 eV for $[Co]_N$ for a *N + NH_3(g) configuration, Fig. 12. Adding the third H atom to the $*N_2H_2$ intermediate to form $*N_2H_3$ is calculated to be the most exergonic step for the distal pathway (Fig. 12A), and thus as with the previous studies of vanadium oxynitrides, the stability of the diazenide intermediate emerges as a critical factor in the NRR mechanism.

In conclusion, calculations suggest that zb-CoN and zb-CoO_xN_y models yield similar geometries for the different N_aH_b surface intermediates, which implies that differences in their relative energetics are due to factors other than geometry, *e.g.*, acid/base properties imparted to N_aH_b by the surface cobalt ions, which are thus dictated by the Lewis acidity of the cationic cobalt active site, and the degree of π-backbonding from the surface metal ions to the bound dinitrogen.

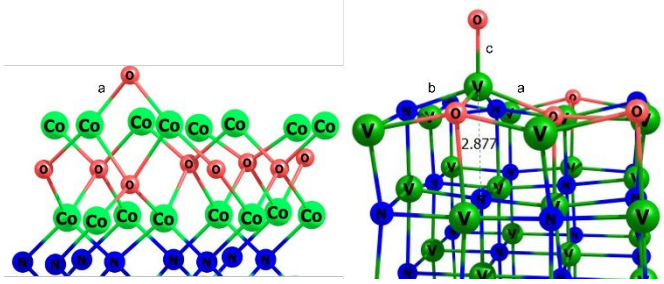

Figure 13 - Co-O (a = 1.77 Å), V-O (a = 1.62 Å, c = 2.10 Å) and V-N (b = 1.97 Å) bond length for CoO_xN_y-O and VO_xN_y-O in NRR.

3.5 Selectivity evaluation of NRR versus HER

Besides high stability and activity, an ideal catalyst for N_2 fixation should be able to reach high Faradaic efficiency for ammonia production and effectively suppress HER activity. Therefore, via the study of other surface configurations, our calculations sought to address catalyst selectivity. The HER process – like NRR – also involves PCET steps and is proposed to occur through Volmer-Heyrovsky or Volmer-Tafel mechanisms.[37] A proton-based HER mechanism involves proton coupled-electron transfer on the surface of the catalyst, producing a surface-bound hydride (H*), *i.e.*, the Volmer step, $H_3O^+ + e^- + * \rightarrow *H + H_2O$. The adsorbed *H interacts with another proton in the solution, the Heyrovsky mechanism: $*H + H_3O^+ + e^- \rightarrow * + H_2O + H_2(g)$. Alternatively, two adsorbed *H can recombine, *viz* the Tafel mechanism: $*H + *H \rightarrow 2* + H_2(g)$

Table 3 - Energetics of HER steps (in eV) for zb-CoO_xN_y and zb-CoN model surfaces.

Step	Name	Equation	E_{rel} for CoN (eV)	E_{rel} for $CoO_{0.44}N_{0.56}$ (eV)
1	Volmer step	$2* + H_2O (g) \rightarrow *H + *OH$	-1.75	-2.83
		$H_2O (g) + * \rightarrow *OH_2$	-0.68	-0.93
		$* + *OH_2 \rightarrow *OH + *H$	-1.08	-1.91
2	(A) Heyrovsky	$*H + H_2O (g) \rightarrow H_2 (g) + *OH$	-0.20	-0.22
	(B) Tafel	$*H + *H \rightarrow H_2 (g) + 2*$	+1.55	+2.61

The DFT results in Table 3 show that the formation of *H is highly favorable (-0.78 eV and -1.31 eV, respectively, eqs. iii and iv) and thus competitive with the formation of $*N_2$ at $[Co]_O$ and $[Co]_N$ surface sites. Hence, calculations suggest that *H may exist in high concentrations on the surface of cobalt oxynitride catalysts and thus inhibit NRR. Moreover, the Volmer step, *i.e.*, scission of water to form *H/*OH (Table 3) is more favorable (-1.91 eV for the zincblende Co oxynitride surface model versus -1.08 eV for the zincblende Co nitride surface model, Table 3). The differences in reaction energies (2.83 eV for $[Co]_O$ versus 1.75 eV for $[Co]_N$) suggest that the Heyrovsky mechanism is more favorable than the Tafel mechanism for these cobalt-based catalysts.

iii. zb-CoN + ½ H_2 (g) → zb-CoN-H

iv. zb-$CoO_{0.44}N_{0.56}$ + ½ H_2 (g) → zb-$CoO_{0.44}N_{0.56}$-H

Another potential problem for NRR on cobalt oxynitrides is the oxidation of the metal centers, given that the $[Co]_O$ and $[Co]_N$ surfaces might be blocked with $*OH_2$, *OH, and *O under the aqueous NRR conditions. To assess this potential problem, calculations on the possible intermediates (by hydrogenating $O* + {}^1/_2 H_2 \rightarrow OH*$ and $*OH + {}^1/_2 H_2 \rightarrow *OH_2$) were performed (Table 4).

Table 4 - Adsorption energy (in eV) of dinitrogen, water on the surface for zb-CoO_xN_y and zb-CoN surface models.

	Co-terminated of zb-CoN	Co-terminated of zb-CoO_xN_y
Name	E_{rel} (eV)	E_{rel} (eV)
$*N_2$	-0.83	-1.24
$*OH_2$	-0.68	-0.93
*OH	-0.30	-0.60
*O	1.10	0.66

DFT calculations suggest that going from CoN to CoO_xN_y, the binding energy of both dinitrogen and water increases, but the increase is more for dinitrogen (ΔE = -0.41 eV) than water (ΔE = -0.25 eV), as shown in Table 4. Regardless, the calculations indicate that N_2 is bonded more tightly than water, which is interesting in light of the experimentally observed greater HER than NRR activity of the cobalt oxynitride catalysts. However, the exchange energies are small, +0.15 eV (~ 3 kcal/mol) for CoN and +0.31 eV (~ 6 kcal/mol) for $CoO_{0.44}N_{0.56}$, and presumably, there is only a small concentration of N_2 in solution due to its limited solubility. On the one hand, the cobalt cation strengthens adsorption of N_2 due to unoccupied d orbitals receiving electrons from the 3σ molecular orbitals of N_2, *i.e.*, sigma-donation in the Dewar-Chatt-Duncanson model.[38] On the other hand, the 2π* orbital of N_2 is partially hybridized with cobalt d orbitals near the Fermi level resulting in π-backdonation of electrons from occupied cobalt d orbitals. Assuming the latter is more significant, as dinitrogen is a very poor Lewis base, the adsorbed N_2 is likely to be partially reduced relative to free dinitrogen, consistent with the computed lengthening of nitrogen-nitrogen bond lengths upon the coordination of dinitrogen to the surface cobalt ions (Fig. 11) and thus more susceptible to protonation upon coordination to the surface. Since dinitrogen can be both a σ-donor and a π-acid, and water is just a σ-donor, we hypothesize that cobalt oxynitride can better π-backdonate, given its slightly higher Fermi energy versus CoN (ΔE_f = 0.04 eV). Given the results for the binding of water, Table 5, which is a σ-only ligand, one might conclude that cobalt oxynitride is more adept than CoN for both σ donation (Lewis acidity) and π-backdonation (π-basicity), so that both the acidity and basicity of the cobalt ion sites are critical factors in not only NRR but HER and thus both activity and selectivity of this family of catalysts.

Table 5 - Calculated energies (in eV) for reaction relevant to HER for rs-VO_xN_y, zb-CoN and zb-CoO_xN_y surface models.

#	Equation	rs-VO_xN_y	zb-CoN (eV)	zb-$CoO_{0.44}N_{0.56}$ (eV)
1	* + H_2O (g) → *OH_2	-0.38	-0.68	-0.93
2	* + *OH_2 → *OH+*H	0.10	-1.08	-1.91
3	*OH + *H→*O + * + H_2 (g)	-0.09	1.87	1.97
4	*OH_2 → H_2 (g)+*O	0.01	0.79	0.06
5	* + ½ O_2 → *O	-2.94	-2.45	-3.43
6	* +½ H_2 (g) → *H	-0.09	-0.78	-1.31
7	2 *OH → 2 *O + H_2 (g)	-3.50	2.19	1.33
8	*H + H_2O (g) → H_2 (g) + *OH	-0.65	-0.20	-0.22

3.6 Comparing VO_xN_y and CoN/CoO_xN_y models

The water/dinitrogen exchange energy on Co nitride/oxynitride models (zb-CoN: +0.15 eV; zb-$CoO_{0.44}N_{0.56}$: +0.31 eV) is more than for rs-VO_xN_y models (-0.32 eV). This suggests that dinitrogen is more stable on cobalt oxynitride than is water, but that the opposite is the case for vanadium oxynitride models. Our experiments (*vide supra*) suggest that VO_xN_y materials are less active for HER than the corresponding CoO_xN_y materials (at least at pH ≥ 7). From the computed energetics in Table 5, it is predicted that the bonding of water to the vanadium oxynitride surface is less favorable for the vanadium oxynitride model (-0.38 eV) versus the two cobalt models (-0.68 for cobalt nitride and -0.93 for cobalt oxynitride). Additionally, while scission of the O—H bond of water is highly favorable for the cobalt systems (-1.08 eV for CoN and -1.91 eV for CoO_xN_y), it is mildly uphill for the vanadium oxynitride model (+0.10 eV, Table 5). Hence, these factors may retard HER in the vanadium systems relative to cobalt congeners.

Moreover, energy values relevant for the formation of *O (line 5 in Table 5) for the TMON models are *ca.* 0.5 eV in favor of the cobalt oxynitride, Table 5, which may be due to the terminal structure of *O for the rs-VO_xN_y model versus the bridging linkage isomer for the zb-CoO_xN_y (Figure 13). Finally, it is also worth noting in the context of relative HER activity that surface hydride formation is considerably more favorable for zb-CoO_xN_y (-1.31 eV) versus rs-VO_xN_y (-0.09 eV), Table 5. We posit that the difference in metal coordination numbers may also play a role in *O and *H stability, and thus HER activity, but further calculations are needed to probe this hypothesis.

3.7 The impact of cobalt formal oxidation state on N_2 binding

The experimental results disclosed above, plus reported experimental results that show enhanced NRR activity upon aluminum doping of Co_3O_4 [19], indicate that the formal oxidation state of the surface cobalt ions is a key factor NRR activity. To probe the impact of cobalt formal oxidation state upon the binding of dinitrogen, Gaussian-based DFT simulations with molecular models were conducted. The calculations utilized the Gaussian 16 code,[39] the PBE0 functional,[40] the SBKJC pseudopotentials/valence basis sets,[41,42] (augmented with d polarization functions on main group elements), and a continuum (SMD) aqueous solvation model.[43] As a simple model of a Co(III) binding site for N_2, a complex $Co(OH)_3(N_2)$ was employed, with triplet spin state. Upon geometry optimization, an NN bond length (r_{NN}) of 1.144 Å and stretching frequency (ν_{NN}) of 2261 cm^{-1} were obtained, Fig.14 (left). These values compare with r_{NN} = 1.141 Å and ν_{NN} = 2353 cm^{-1} for free N_2 at the same level of theory, and are suggestive of only modest N_2 activation upon coordination to the Co(III) site. The $Co(OH)_3(N_2)$ model was then reduced by 1 e^- and the resulting Co(II) complex re-optimized. The predicted r_{NN} and ν_{NN} values are 1.165 Å and 2098 cm^{-1}, respectively, indicative of more significant NN activation upon coordination of dinitrogen to the Co(II) model, Fig. 14 (right).

As the solid-state, plane-wave DFT simulations indicate a preference for bimetallic bonding of N_2, molecular Co(II) models of such were also constructed and geometry optimized as before, Fig. 15. As can be seen from the computed metrics and ν_{NN} of the bimetallic $Co(II)_2$ model, there is enhanced cooperative activation of N_2 by multiple Co(II) sites versus a single Co(II) site (*cf.* Fig. 14, right), thus one may presume that surface morphology, in particular the separation between surface metal sites and thus their ability to participate in cooperative binding of N_2 and the intermediates generated by its reduction, may be another key factor in NRR activity.

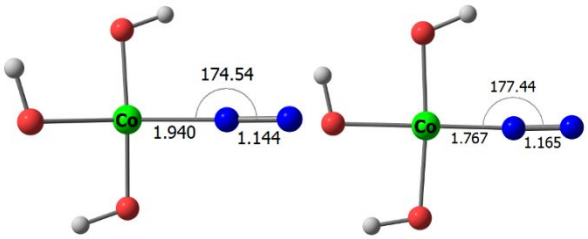

Figure 14 - PBE0/CEP-31G(d)/SMD-water optimized geometries of molecular Co (III) – left – and Co (II) – right – models of a $[Co]_O$ site in CoO_xN_y. Light green, red, grey and blue spheres represent Co, O, H and N atoms, respectively.

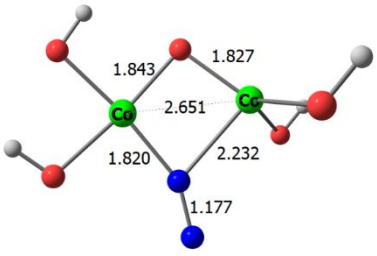

Figure 15 - PBE0/CEP-31G(d)/SMD-water optimized geometry of a molecular Co $(II)_2$ model of $[Co]_O$ sites in CoO_xN_y. Light green, red, grey and blue spheres represent Co, O, H and N atoms, respectively.

4. Summary and Conclusions

Experimental studies combining electrochemical methods (voltammetry, fluorescence, absorption spectroscopy, and gas chromatography), combined with *ex-situ* XPS and DFT simulations, demonstrate that oxygen-rich cobalt oxynitride films ($CoO_{0.8}N_{0.2}$) are both NRR and HER active at pH 10, with both lattice N and solvated N_2 being reduced to NH_3 without evidence of N_2 incorporation as lattice N – as would be expected in an MVK mechanism. In contrast, V oxynitride films ($VO_{0.4}N_{0.6}$) are both HER and NRR inactive at pH 10, and NRR active/HER inactive at pH 7. These results are summarized in Table 6.

Table 6. Summary of V and Co oxynitride NRR, HER behaviors

Material	pH	NRR (N_2-saturated	NRR (Ar-saturated	HER
$VO_{0.4}N_{0,6}$	7	Active	Active	Inactive
$VO_{0.4}N_{0,6}$	10	Inactive	Inactive	Inactive
$CO_{0,8}N_{0.2}$	10	Active	Active	Active

Although it might be argued that this comparison is somewhat incomplete, in that V oxynitride films are somewhat more N-rich than the examined Co oxynitride films, recent experiments indicate that pure VN films are NRR inactive, [44] while our previous studies of V oxynitride films for NRR at pH 7 indicate similar behavior over a range of N/O compositions, including N-free V oxides (i.e., enhanced NRR activity for O-rich VO_xN_y).

The experimental data further show that Co oxynitride films are far more active for HER than for NRR under the conditions tested (Fig. 4), and that both lattice N and solvated N_2 are reduced to NH_3 without evidence of solvated N_2 being incorporated as lattice N. Indeed, as shown in Fig. 5, N is rapidly removed from the Co oxide lattice, leaving NRR active Co(II) oxide. In this respect, the NRR behavior of Co oxynitride at pH 10 is similar to that of V oxynitride at pH 7 – a gradual loss of lattice N due to reduction to NH_3, leaving an oxide lattice that is still NRR active.[15]

The absence of an MVK mechanism for Co oxynitride – as demonstrated in the present research – and previously demonstrated for V oxynitride[15] demonstrates that lattice N will eventually be depleted from the Co or V oxynitride lattice. Given the demonstrated NRR activity of both CoO (Table 1) and V oxide,[26] these data suggest that any advantage of lattice N in terms of overall NRR efficiency or selectivity in these two systems is only transient. A key point, therefore, in future studies of TMON systems, therefore, should be improved understanding of the overall stability of lattice N under NRR conditions.

The HER activity observed for Co oxynitride (pH 10) and HER inactivity for V oxynitride (pH 7 and pH 10), are further complemented by the computational results. The adsorption and dissociation of water at $[Co]_O$ sites are quite favorable, and cobalt oxide is well known as an HER (and OER) catalyst under alkaline conditions.[45] In contrast, O-H bond scission is calculated to be uphill for H_2O adsorbed at V cation sites, suggesting that H_2O adsorption or OH adsorption at such sites under neutral or alkaline conditions would block HER activity. Indeed, the reported HER activity of V oxide under acidic conditions is also consistent with our experimental and theoretical results, indicating that HER at a vanadium oxide (or oxynitride surface) proceeds by a proton-initiated mechanism, as previously concluded. [37] These data lead us to hypothesize that hydroxide adsorption at V cation sites inhibits N_2 adsorption, and resulting in the experimentally observed NRR and HER inactivity of V oxynitride at pH 10.

Further, experiment and theory demonstrate that Co oxynitride is both NRR and HER active at pH 10, but upon the loss of lattice N, yielding a Co(II) oxide that is still NRR active. Moreover, maintenance of the Co in the 2+ formal oxidation state seems critical for NRR activity. The HER reaction, however, proceeds at a far higher rate than NRR under these conditions. In contrast, V oxynitride, at pH 10, is inactive for both NRR and HER. At pH 7, V oxynitride is active for NRR and inactive for HER.

In conclusion, the experimentally-determined trends in NRR/HER activities for V oxynitride at pH 7 and 10, and for Co oxynitride at pH 10, are summarized in Table 6. Theoretical calculations indicate that these trends are explained by the following factors:

(i) strong OH^- and H_2O adsorption at V cation sites, coupled with less favourable O-H bond scission energetics, and

(ii) different HER mechanisms for V and Co oxynitrides, with proton adsorption as an initial step for the former and H_2O adsorption on the latter.

These results suggest that electrocatalytic differences are due to enhanced oxophilicity of V cation sites relative to Co cation sites and that similar trends in NRR/HER selectivity vs. pH may be observed for other early transition metal oxynitrides. Corresponding experiments are in progress in our laboratories.

Conflicts of interest

There are no conflicts to declare.

Acknowledgments

The authors gratefully acknowledge the support of this work by the National Science Foundation through the grant DMR-2112864 (to J.A.K., T.R.C., and F.D.) Additional NSF support for the UNT CASCaM HPC cluster via Grant CHE-1531468 is also gratefully acknowledged. T.R.C. and M.G. thank the NSF for partial support of this research via grant CHE-1953547.

References

1 J. Chen, H. Cheng, L. Ding and H. Wang, *Mater. Chem. Front.,* 2021, **5**, 5954-5969.

2 G. Qing, R. Ghazfar, S. T. Jackowski, F. Habibzadeh, M. M. Ashtiani, C. Chen, M. R. Smith and T. W. Hamann, *Chem. Rev.,* 2020, **120**, 5437-5516.

3 J. Hou, M. Yang and J. Zhang, *Nanoscale,* 2020, **12**, 69-692.

4 C. Smith, A. K. Hill and L. Torrente-Murciano, *Energy Environ. Sci.,* 2020, **13**, 331-344.

5 Q. Liu, T. Xu, Y. Luo, Q. Kong, T. Li, S. Lu, A. A. Alshehri, K. A. Alzahrani and X. Sun, *Curr. Opin. Electrochem.,* 2021, **29**, 100766.

6 J. Humphreys, R. Lan and S. Tao, *Adv. Energy Sustainability Res.,* 2021, **2**, 2000043.
7 A. R. Singh, B. A. Rohr, M. J. Statt, J. A. Schwalbe, M. Cargnello and J. K. Nørskov, *ACS Catal.,* 2019, **9**, 8316-8324.
8 J. Pan, H. A. Hansen and T. Vegge, *J. Mater. Chem. A: Mater. Energy Sustainability,* 2020, **8**, 2498-2417.
9 F. Hanifpour, C. P. Canales, E. G. Fridriksson, A. Sveinbjörnsson, T. K. Tryggvason, E. Lewin, F. Magnus, Á S. Ingason, E. Skúlason and H. D. Flosadóttir, *Electrochim. Acta,* 2022, **403**, 139551.
10 B. Chang, L. Deng, S. Wang, D. Shi, Z. Ai, H. Jiang, Y. Shao, L. Zhang, J. Shen, Y. Wu and X. Hao, *J. Mater. Chem. A: Mater. Energy Sustainability,* 2019, **8**, 91-96.
11 S. Kang, J. Wang, S. Zhang, C. Zhao, G. Wang, W. Cai and H. Zhang, *Electrochem. Commun.,* 2019, **100**, 90-95.
12 Y. Yao, Q. Feng, S. Zhu, J. Li, Y. Yao, Y. Wang, Q. Wang, M. Gu, H. Wang, H. Li, X. Yuan and M. Shao, *Small Methods,* 2019, **3**, 1800324.
13 X. Yang, S. Kattel, J. Nash, X. Chang, J. H. Lee, Y. Yan, J. G. Chen and B. Xu, *Angewandte Chem. (International ed.),* 2019, **58**, 13768-13772.
14 L. Niu, L. An, X. Wang and Z. Sun, *J. Energy Chem.,* 2021, **61**, 304-318.
15 A. Osonkie, A. Ganesan, P. Chukwunenye, F. Anwar, K. Balogun, M. Gharaee, I. Rashed, T. R. Cundari, F. D'Souza and J. A. Kelber, *ACS Appl. Mater. Interfaces,* 2022, **14**, 531-542.
16 D. Ologunagba and S. Kattel, *Mater. Adv.,* 2021, **2**, 1263-127.
17 B. H. R. Suryanto, H. Du, D. Wang, J. Chen, A. N. Simonov and D. R. MacFarlane, *Nat. Catal.,* 2019, **2**, 290-296.
18 B. M. Ceballos, G. Pilania, K. P. Ramaiyan, A. Banerjee, C. Kreller and R. Mukundan, *Curr. Opin. Electrochem.,* 2021, **28**, 100723.
19 X. Lv, Y. Liu, R. Hao, W. Tian and Z. Yuan, *ACS Appl. Mater. Interfaces,* 2020, **12**, 17502-17508.
20 K. Chu, Y. Liu, Y. Li, H. Zhang and Y. Tian, *J. Mater. Chem. A: Mater. Energy Sustainability,* 2019, **7**, 4389-4394.
21 F. Faisal, M. Bertram, C. Stumm, S. Cherevko, S. Geiger, O. Kasian, Y. Lykhach, O. Lytken, K. J. J. Mayrhofer, O. Brummel and J. Libuda, *J. Phys. Chem. C,* 2018, **122**, 7236-7248.
22 F. Faisal, C. Stumm, M. Bertram, T. Wähler, R. Schuster, F. Xiang, O. Lytken, I. Katsounaros, K. J. J. Mayrhofer, M. A. Schneider, O. Brummel and J. Libuda, *PCCP,* 2018, **20**, 23702-23716.
23 F. Faisal, C. Stumm, M. Bertram, F. Waidhas, Y. Lykhach, S. Cherevko, F. Xiang, M. Ammon, M. Vorokhta, B. Šmíd, T. Skála, N. Tsud, A. Neitzel, K. Beranová, K. C. Prince, S. Geiger, O. Kasian, T. Wähler, R. Schuster, M. A. Schneider, V. Matolín, K. J. J. Mayrhofer, O. Brummel and J. Libuda, *Nat Mater.,* 2018, **17**, 592-598.
24 A. Osonkie, V. Lee, A. Oyelade, M. Mrozek-McCourt, P. Chukwunenye, T. D. Golden, T. R. Cundari and J. A. Kelber, *PCCP,* 2020, **22**, 2464-24648.
25 A. Osonkie, V. Lee, P. Chukwunenye, T. Cundari and J. Kelber, *J. Chem. Phys.,* 2020, **153**, 144709.
26 A. Ganesan, A. Osonkie, P. Chukwunenye, I. Rashed, T. R. Cundari, F. D'Souza and J. A. Kelber, *J. Electrochem. Soc.,* 2021, **168**, 26504.
27 B. Dong, A. Oyelade, N. Nandagopal and J. A. Kelber, *Surf. Coat. Technol.,* 2017, **314**, 45-50.
28 M. Seah and D. Briggs, *Practical Surface Analysis. Volume 1. Auger and X-ray photoelectron spectroscopy*, Wiley and Sons: New York, 1990.
29 M. C. Biesinger, B. P. Payne, A. P. Grosvenor, L. W. M. Lau, A. R. Gerson and R. S. C. Smart, *Appl. Surf. Sci.,* 2011, **257**, 2717-2730.
30 R. M. Holmes, A. Aminot, R. Kérouel, B. A. Hooker and B. J. Peterson, *Can. J. Fish. Aquat. Sci.,* 1999, **56**, 1801-1808.
31 J. Hafner, *J. Comput. Chem.,* 2008, **29**, 2044-2078.
32 G. Kresse and D. Joubert, *Phys. Rev. B: Condens. Matter,* 1999, **59**, 1758-1775.
33 H. J. Monkhorst and J. D. Pack, *Phys. Rev. B,* 1976, **13**, 5188.
34 M. Gudmundsson, V. Ellingsson, E. Skúlason and Y. Abghoui, *Top Catal,* 2021, **65**, 252-261.
35 O. Olanipekun, C. Ladewig, J. A. Kelber, M. D. Randle, J. Nathawat, C. Kwan, J. P. Bird, P. Chakraborti, P. A. Dowben, T. Cheng and W. A. Goddard, *SST,* 2017, **32**, 95011.
36 S. Tanuma, C. J. Powell and D. R. Penn, *Surf. Interface Anal.,* 2003, **35**, 268-275.
37 K. K. Dey, S. Jha, A. Kumar, G. Gupta, A. K. Srivastava and P. P. Ingole, *Electrochim. Acta,* 2019, **312**, 89-99.
38 N. Mézailles, in *Transition Metal-Dinitrogen Complexes, Preparation and Reactivity*, ed., 2019, p. 221-269.
39 M. J. Frisch, G. W. Trucks, H. B. Schlegel, G. E. Scuseria, M. A. Robb, J. R. Cheeseman, G. Scalmani, V. Barone, G. A. Petersson, H. Nakatsuji, X. Li, M. Caricato, A. V. Marenich, J. Bloino, B. G. Janesko, R. Gomperts, B. Mennucci, H. P. Hratchian, J. V. Ortiz, A. F. Izmaylov, J. L. Sonnenberg, D. Williams-Young, F. Ding, F. Lipparini, F. Egidi, J. Goings, B. Peng, A. Petrone, T. Henderson, D. Ranasinghe, V. G. Zakrzewski, J. Gao, N. Rega, G. Zheng, W. Liang, M. Hada, M. Ehara, K. Toyota, R. Fukuda, J. Hasegawa, M. Ishida, T. Nakajima, Y. Honda, O. Kitao, H. Nakai, T. Vreven, K. Throssell, J. A. Montgomery, Jr., J. E. Peralta, F. Ogliaro, M. J. Bearpark, J. J. Heyd, E. N. Brothers, K. N. Kudin, V. N. Staroverov, T. A. Keith, R. Kobayashi, J. Normand, K. Raghavachari, A. P. Rendell, J. C. Burant, S. S. Iyengar, J. Tomasi, M. Cossi, J. M. Millam, M. Klene, C. Adamo, R. Cammi, J. W. Ochterski, R. L. Martin, K. Morokuma, O. Farkas, J. B. Foresman, and D. J. Fox, *Gaussian 16, Revision C.01*, Wallingford CT, 2016.
40 C. Adamo and V. Barone, *J. Chem. Phys.,* 1999, **110**, 6158-6170.
41 W. J. Stevens, H. Basch and M. Krauss, *J. Chem. Phys.,* 1984, **81**, 6026-6033.
42 W. J. Stevens, M. Krauss, H. Basch and P. G. Jasien, *Can. J. Chem.,* 1992, **70**, 612-630.
43 Z A. V. Marenich, C. J. Cramer and D. G. Truhlar, *J. Phys. Chem. B,* 2009, **113**, 6378-6396.
44 H. Du, T. R. Gengenbach, R. Hodgetts, D. R. MacFarlane and A. N. Simonov, *ACS Sustainable Chem. Eng.,* 2019, **7**, 6839-6850.
45 H. Jin, J. Wang, D. Su, Z. Wei, Z. Pang and Y. Wang, *J. Am. Chem. Soc.,* 2015, **137**, 2688-2694.
46 G.W. Watt and J. D. Chrisp, *Anal. Chem*. 1952, **24**, 2006-2008.